Article
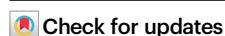
Interfacial electrostatic repulsion inhibits iodide ion migration for enhancing reverse-bias stability of perovskite solar cells

Zhineng Lan, Yingying Yang, Hao Huang ✉, Shuxian Du, Qiang Zhang, Zhiwei Wang, Tongtong Jiang, Changxu Sun, Shujie Qu, Liang Li, Luyao Yan, Peng Cui ⓘ & Meicheng Li ⓘ ✉

The perovskite solar cells (PSCs) achieve notable advances in stability under humidity, light, and heat stress. However, PSCs are still susceptible to reverse-bias degradation, mainly due to the inevitable iodide ions migration. Herein, we reveal the irreversible cross-layer migration of iodide ion (I^-) within PSCs under reverse bias, which contributes to the device performance failure. Further, we innovatively construct an electrostatic repulsion with I^- at the perovskite interface, which can inhibit I^- cross-layer migration under reverse bias in a nonbonding manner. Besides, the TFMS capable of blocking the hole injection can reduce the interface I^- oxidation under reverse bias. The modified PSCs deliver efficiencies of 25.80% with TiO_2 as the electron transport layer (ETL) and 26.21% (certification of 26.09%) with SnO_2 as the ETL. More importantly, the device exhibit an enhanced reverse-bias stability by maintaining >80% of initial efficiency after 25 bias aging cycles (0 V/−1 V/0 V, each stage lasts for 12 hours). Our work provides a route to inhibit ion migration in PSCs and other perovskite-based devices through a novel interaction of electrostatic repulsion.

The metal halide perovskite solar cells (PSCs) have achieved significant advances in photovoltaic performance with a certified power conversion efficiency (PCE) of >27% in single-junction devices and >30% in all-perovskite tandem devices[1–4], thrusting them into the spotlight as a transformative technology under the global pursuit of sustainable energy solutions. However, a vital challenge limiting their industrialization and practical application is stability, especially under the harsh conditions that commonly emerge during practical operation, such as high temperature, ultraviolet (UV) irradiation, and reverse bias voltage[5–10]. Various efforts have been made regarding crystallization regulation, defect engineering, device encapsulation, and so on, to enhance the device stability under heat, humidity, and UV irradiation[11–16]. However, in practical applications, due to the inevitable partial blocking by clouds, leaves, bird droppings, etc., the PSCs undergo a normally overlooked issue of reverse bias, making the reverse-bias stability an urgent issue of PSCs during practical applications[6,9].

As an ionic soft crystal, metal halide perovskite is susceptible to reverse-bias degradation, since the components are prone to migrate as ionic defects under electric bias. When the PSCs undergoing a reverse bias that can be superimposed on the PSC's internal electric field, the relatively weak Pb–I bonds in perovskites are prone to break, generating massive mobile iodide ions (I^-)[17–20]. The accumulation of migrating ions at the electron transport layer (ETL)/perovskite interface will induce the offset of interface energy level and the chemical reaction of perovskite self-accelerating degradation[21–24]. Besides, I^- will further migrate across the interface into ETL, which not only causes irreversible perovskite decomposition but also causes damage to the ETL, resulting in irreversible efficiency decay and even complete failure of PSCs[25–29]. To enhance the reverse-bias stability, efforts such as

State Key Laboratory of Alternate Electrical Power System with Renewable Energy Sources, School of New Energy, North China Electric Power University, Beijing, China. ✉e-mail: hhuang@ncepu.edu.cn; mcli@ncepu.edu.cn

using the grain boundary passivation strategy to reduce the fast channel of ion migration and leveraging the buffer layer to capture I⁻ or inhibit I⁻ migration have been made[24,26,30–35]. Recently, a systematic study on the degradation mechanisms of PSCs under reverse bias reported that the oxidation of iodide by injected holes at the cathode side initializes the reverse-bias-induced degradation, a corresponding strategy of reinforced barrier with multiple layers was proposed to physically and mechanically block the reaction between I⁻ and metal electrodes, which effectively enhances the bias-voltage stability PSCs with an efficiency of 24.5%[20,26]. Although the strategy of interface barrier with the function of physical block is reported to be feasible to enhance device stability, including reverse-bias stability, the barrier layer is normally synthesized on a complicated manner and may sacrifice the high efficiency, which also brings a hindrance to the current mature fabrication process of the efficient device[29,35–37]. Hence, it is highly desirable to find a strategy to enhance the reverse-bias stability while maintaining the high efficiency and being well compatible with current mature technology.

In this work, we propose interfacial electrostatic repulsion distinct from electrostatic attraction or chemical binding to enhance the PSCs reverse-bias stability. We constructed an electrostatic repulsion with I⁻ by incorporating 4,4',4",4"'-methanetetrayltetrabenzenesulfonic acid (TFMS) at the perovskite interface to inhibit the I⁻ cross-layer migration under reverse bias. The TFMS possesses four -SO₃H groups with rich negative charges, which can passivate the interfacial defects and further form an electrostatic repulsion with I⁻. Both theoretical calculations and experimental results demonstrated that the interfacial

electrostatic repulsion between TFMS and iodide ions can effectively inhibit the cross-layer migration of I⁻. Based on this strategy, we obtained champion PCEs of 25.80% on the TiO₂-based planar PSCs and 26.21% (certification of 26.09%) on the SnO₂-based planar PSCs. The modified device also shows enhanced stability by maintaining 91% and 88% of its initial efficiency after aging under ambient conditions for 1400 h and UV light for 1000 h, respectively. Furthermore, based on interfacial electrostatic repulsion, the device exhibited better reverse-bias stability, retaining >80% of initial efficiency after 25 bias aging cycles (0 V/-1 V/0 V, each stage lasting for 12 h) and yielding a breakdown voltage of -28.11 V.

Results and discussion

Construction of interface electrostatic repulsion

The PSCs in the practical application process inevitably suffer the reverse bias due to the partial blocking by clouds, leaves, bird droppings, etc. As an ionic soft crystal, perovskites are susceptible to reverse-bias degradation due to the ion migration under the electric bias, especially the I⁻, which possesses a low migration activation energy. Under the reverse bias, the I⁻ will migrate directionally, and even migrate cross the buried interface, which can be validated by the in-depth X-ray Photoelectron Spectroscopy (XPS) (Fig. 1a and Supplementary Fig. 1). Hence, suppressing the I⁻ migration, especially irreversible cross-layer migration is supposed to be a feasible strategy to enhance the reverse-bias stability. In addition to electrostatic attraction, electrostatic repulsion, as another fundamental physical force, was first constructed to modulate I⁻, which is supposed to
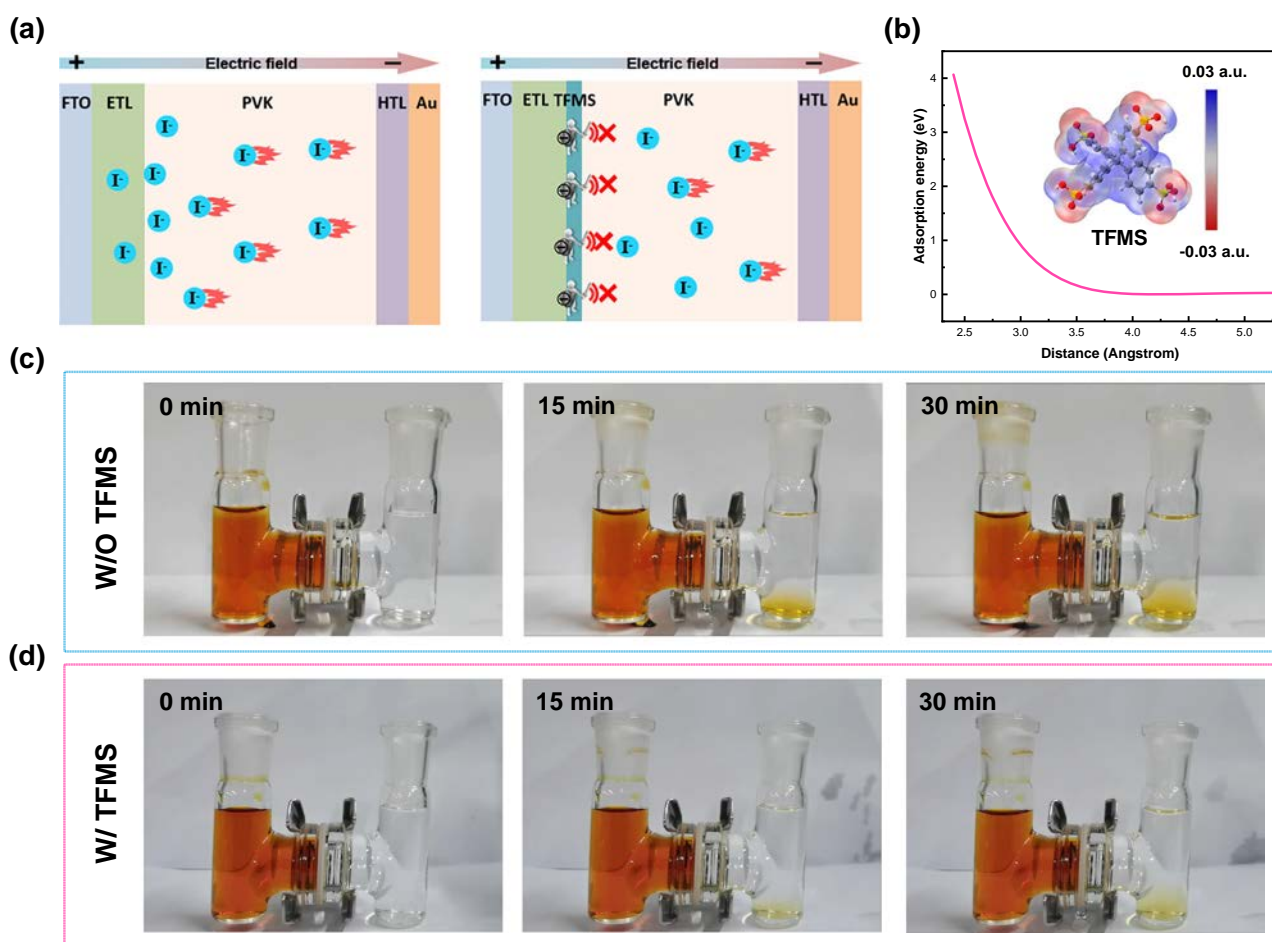
Fig. 1 | Proposal of interface electrostatic repulsion strategy. a Schematic diagram of interfacial electrostatic repulsion inhibiting ion cross-layer migration. b Diagram of binding energy between TFMS and I⁻ with distance, the illustration shows the electrostatic surface potential of TFMS. c, d The diffusion of polyiodide ions when the diaphragm is with TFMS and without TFMS.
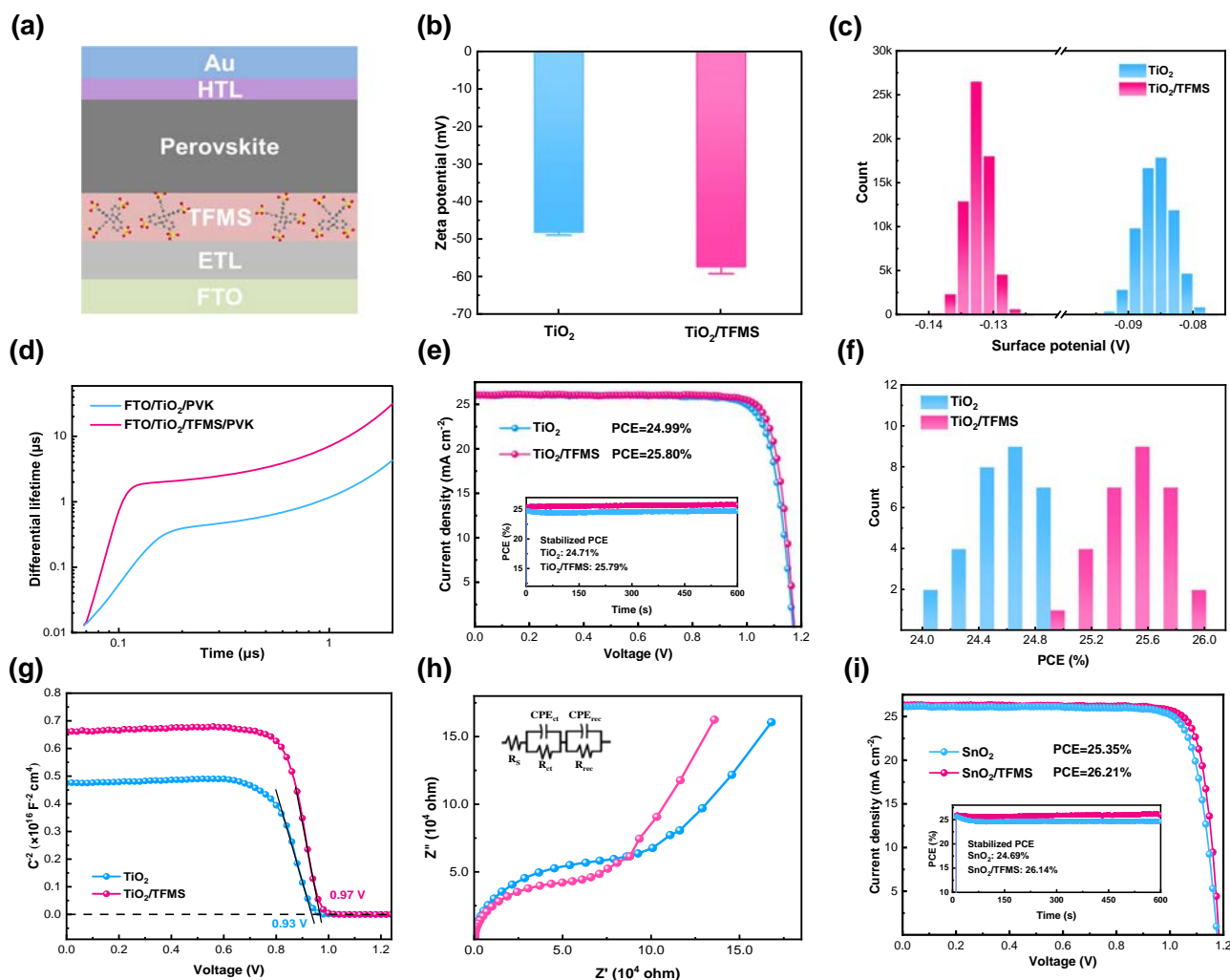
Fig. 2 | Photovoltaic performances of PSCs. a The schematic diagram of PSCs structure. **b** Zeta potential of TiO_2 and TiO_2/TFMS films surface. **c** Surface potential distribution of TiO_2 and TiO_2/TFMS films. **d** Computed differential lifetimes through fitting the TRPL spectra. **e** *J-V* curves (reverse scan) of the champion TiO_2-based and TiO_2/TFMS-based PSCs with an active area of 0.08 cm². The illustration shows the stabilized power output of PSCs. **f** Distribution histograms of PCE of TiO_2-based PSC and TiO_2/TFMS-based PSCs, 30 in each group. **g** The Mott-Schottky curve of PSCs. **h** The EIS curve of PSCs. **i** *J-V* curves (reverse scan) of the champion SnO_2-based and SnO_2/TFMS-based PSCs with an active area of 0.08 cm².

suppress the I^- migration at the interface in a nonbonding and releasable manner (Fig. 1a).

The material 4,4',4",4"'-methanetetrayltetrabenzenesulfonic acid (TFMS, the molecular structure shown in Supplementary Fig. 2 and Fig. 1b) was selected to construct the electrostatic repulsion with I^- at the interface[33,38–40]. TFMS has four sulfonic acid groups ($-SO_3H$) connected to four benzene rings respectively, and four benzene rings connected to one central carbon atom, delivering a three-dimensional structure. These sulfonic acid groups are highly electronegative due to the strong electron-withdrawing nature of the sulfur atom, which is bonded to three oxygen atoms. The oxygen atoms in the sulfonic acid groups have high electronegativity, pulling electron density away from the benzene rings and creating a partial positive charge on the carbon atoms to which they are attached. At the same time, the four benzene rings in the whole molecule of TFMS are connected by a carbon atom, forming a large conjugated system, which increases the degree of delocalization of electrons, leading to an overall high electronegativity for the compound[41]. This high electronegativity of the $-SO_3H$ group has been confirmed by the calculation of electrostatic potentials (Fig. 1b). To prove the repulsive effect between TFMS and I^-, we simulated the evolution of adsorption energy between I^- and TFMS as the I^- approaches the $-SO_3H$ group. The results show that the adsorption energy

becomes larger as the distance between the two gets closer, indicating that I^- will be subject to electrostatic repulsion when it moves toward TFMS (Fig. 1b). An experiment of polyiodide ion diffusion was designed to intuitively display the repulsion effect of TFMS on polyiodide ions (Supplementary Fig. 3, Tables S1 and S2). It is noted that the incorporated TFMS shows negligible influence on the morphologies and structures of diaphragms. As shown in Fig. 1c and d, the diffusion of polyiodide ions can be effectively hindered by incorporating the TFMS into the diaphragm, which can be validated by the lighter color of the solution on the right side[39,40,42]. This repulsion between TFMS and polyiodide ions, and its effect on hindering the diffusion of polyiodide ions, is going to be further constructed and discussed in PSCs, with the aim of enhancing their reverse-bias stability.

Photovoltaic performances of PSCs

The TFMS was introduced into the interface of TiO_2/perovskite (Fig. 2a). The appearance of the S *2p* peak and the offset of the Ti *2p* peak in the XPS results show that TFMS is successfully introduced and bonded on the surface of TiO_2 (Supplementary Fig. 4). In addition, the TFMS has been confirmed to show negligible effect on TiO_2 surface morphology (Supplementary Fig. 5 and 6). However, after introducing the TFMS, the surface wettability is improved (Supplementary Fig. 7),

which is conducive to the subsequent deposition of perovskite films (Supplementary Fig. 8–10). Combined with the measurements of the Zeta potential, Kelvin probe force microscopy (KPFM), and ultraviolet photo-electron spectroscopy (UPS) (Figs. 2b, c and Supplementary Fig. 11–13), it can be observed that the TFMS effectively decreases the surface potential of TiO_2 and optimize the interfacial energy level. Based on TRPL spectrum (Supplementary Fig. 14), we further calculated the differential lifetime (Fig. 2d)[43,44]. The early charge transfer process leads to a sharp increase in differential lifetime, reflecting the speed of charge transfer. In contrast, the greater slope of TiO_2/TFMS sample indicates that the transfer speed of electrons to the fluorine-doped tin oxide (FTO) electrode is significantly faster. This promoted interfacial electron extraction can also be validated by the measurement of transient photocurrent, in which the TiO_2/TFMS-based PSCs show a smaller photocurrent decay time (Supplementary Fig. 15). In addition, the reduced interface trap density can be demonstrated by the measurement of space charge limited current (SCLC) (Supplementary Fig. 10). The accelerated electron transfer and reduced interfacial defects after incorporating TFMS are expected to improve the PSCs efficiency. We prepared PSCs structured as FTO/TiO_2 (TFMS)/perovskite/ 2,2′,7,7′-Tetrakis [N,N-di(4-methoxyphenyl)amino]-9,9′-spirobifluorene (Spiro-OMeTAD)/Au. Figure 2e shows the current density voltage (J-V) curve (reverse scan) and steady-state output power of the best-performing PSCs with an active area of 0.08 cm^2. The TiO_2/TFMS-based PSCs achieve a PCE of 25.80% with a stabilized power output (SPO) of 25.79% after tracking 600 s, while the TiO_2-based PSCs have a PCE of 24.99% with a SPO of 24.71%. The improvement should be attributed to the promoted interfacial carrier transport and reduced interface carrier recombination. The corresponding external quantum efficiency (EQE) spectrum of TiO_2/TFMS-based PSCs was shown in Supplementary Fig. 16, in which the integrated current density yields a small variation with the value obtained from J-V measurement. Meanwhile, we calculated the hysteresis factor of TiO_2/TFMS-based PSC to be 0.78%, which is smaller than the 4.40% of TiO_2-based PSC, suggesting the promoted interfacial electron transport and suppressed ion migration (Supplementary Fig. 17 and Table S3). A batch of PSCs was prepared to evaluate the reproducibility of high efficiency. As shown in Fig. 2f, both type of PSCs shows satisfying reproducibility. In detail, the TiO_2/TFMS-based PSCs exhibit an average PCE of 25.44%, which is higher than that (24.60%) of TiO_2-based PSCs (Supplementary Fig. 18).

Additionally, the physical property of PSCs with and without TFMS was further investigated through various measurements. Mott-Schottky tests show that the TiO_2/TFMS-based PSC exhibits a higher built-in field (V_{bi}) of 0.97 V, indicating the promoted separation of electron-hole pairs and transport of carriers (Fig. 2g). In addition, electrochemical impedance spectroscopy (EIS) tests in the dark state were carried out to characterize the carrier dynamics in PSCs (Fig. 2h). The TiO_2/TFMS-based PSC exhibits a lower contact resistance and higher recombination resistance, indicating that the TFMS is conducive to reducing carrier recombination, which is further verified by the reduced dark current and the smaller ideal factor (n_{ID}) after introducing TFMS (Supplementary Figs. 19 and 20).

The effectiveness of TFMS in improving the photovoltaic performance of PSCs was also validated by using SnO_2 as the ETL. Notable, the best-performing SnO_2/TFMS-based PSCs achieved a PCE of 26.21% in reverse scan and 26.05% in forward scan (Fig. 2i, and Supplementary Fig. 21, and Table S4). In comparison, the SnO_2-based PSCs achieved a PCE of 25.35% in the reverse scan and 24.70% in the forward scan. The SPO after tracking 600 s of SnO_2/TFMS-based PSCs is 26.14%, higher than that (24.69%) of SnO_2-based PSCs. Encouragingly, one of the best-performing SnO_2/TFMS-based PSCs was sent to a third-party institute (National Institute of Metrology, China) for certification, obtaining a certified PCE of 26.09% (Supplementary Fig. 22). Statistical analyses on 25 individual devices with or without TFMS were summarized. The

SnO_2/TFMS-based PSCs achieved 25.44% on average compared with 24.78% for the SnO_2-based PSCs (Supplementary Fig. 23). These results of TiO_2-based PSCs and SnO_2-based PSCs jointly demonstrate that the TFMS at ETL/perovskite interface can effectively improve the photovoltaic performance.

Interface electrostatic repulsion improves PSCs' reverse bias stability

To investigate the influence of interfacial electrostatic repulsion on the I^- migration under reverse bias, several experiments have been designed and carried out. Firstly, we performed an in-depth XPS measurement on the FTO substrate after the corresponding device aged under -1 V bias for 2 h. We peeled off the perovskite film using a reported method and then obtained XPS spectra of FTO every 100 s of etching (Supplementary Fig. 24). Both samples show obvious I 3d peaks before etching, indicating the presence of residual perovskite on the FTO surface after the peeling-off method (Fig. 3a and b). After etching for 100 s, the Sn 3d peak of both samples shows obvious enhancement and reaches a relatively stable intensity, indicating that the measuring position has entered the FTO substrate (Supplementary Fig. 25). In this depth, the FTO for the control sample still shows an I 3d peak, and the intensity of this peak gradually decreases as the prolongs of etching time, indicating that I^- migrated across the interface into the FTO substrate. On the contrary, the substrate for the sample with TFMS shows no signal of I element even after etching for 100 s, demonstrating that the TFMS can effectively inhibit the I^- cross-layer migration under reverse bias. The inhibited I^- cross-layer migration has been further validated by the test of the time of flight secondary ion mass spectrometry (ToF-SIMS) on the PSCs after aging at -1 V bias for 2 h. As shown in Fig. 3c and Supplementary Fig. 26, compared to the I^- in TiO_2/TFMS-based PSC, the I^- in TiO_2-based PSC shows a migration forwarding to ETL side, accompanied by the more generation of I_3^-, demonstrating the reversed bias-induced I^- migration can be inhibited by the TFMS. We further use DFT calculations to investigate the interaction between TFMS and perovskite[45,46]. The different mapped colors of the sign(λ_2)ρ function indicators can be used to clearly show the form of interactions within the region, with the red indicating prominent repulsion interaction, the green indicating van der Waals interaction, and the blue indicating weak interaction. As shown in Fig. 3d and Supplementary Fig. 27, the sulfonic acid group in TFMS near the iodide ion shows a red color, which indicates an obvious prominent repulsion interaction. At the same time, a perovskite model was constructed to calculate the migration path and barrier of I^- migration. The energy barrier of I^- migrating away from the surface of perovskite without the TFMS was calculated to be 0.346 eV (Fig. 3e, f). When TFMS was introduced on the perovskite surface, the energy barrier of iodide migrating away from perovskite increased to 0.680 eV, indicating that the TFMS can effectively hinder the I^- cross-layer migration. The above experimental and theoretical results reveal that the TFMS can form electrostatic repulsion with I^-, which increases the energy barrier of I^- migration in a nonbonding manner, effectively inhibiting I^- cross-layer migration under reverse bias (Supplementary Fig. 28).

The device stability under reverse bias was also comprehensively researched. Under long-term reverse bias, the continuous I^- migration induces the degradation of perovskite materials at the interface (Fig. 4a). In contrast, the reverse bias-induced perovskite decomposition has been suppressed in TiO_2/TFMS-based PSC, indicating enhanced reverse-bias stability after incorporating the TFMS. We also tested the dark state current of the PSCs before and after aging under -1 V bias for 100 h. The dark state current of the TiO_2-based PSCs significantly increased by about 10 times, while the dark current of the TiO_2/TFMS-based PSCs only increased by about 2 times (Fig. 4b). The significant increase in dark current is due to the presence of massive shunt paths in the device, which should be related to the reverse bias-
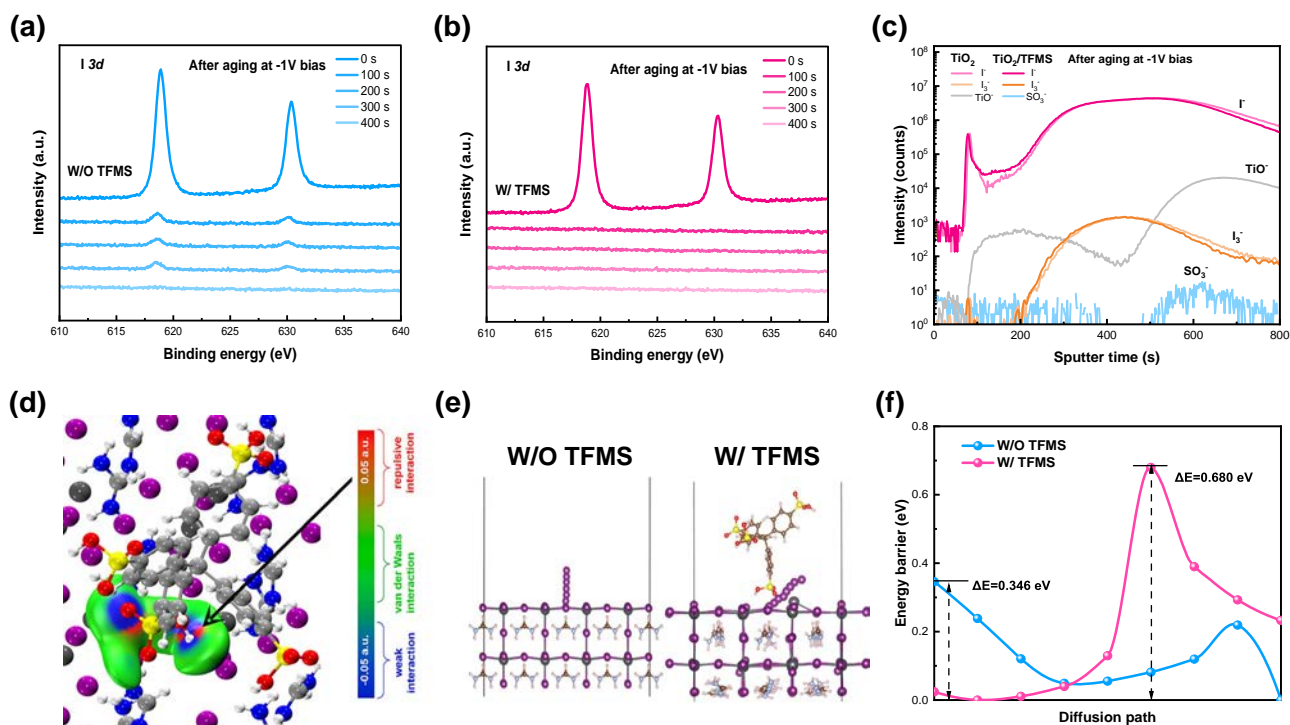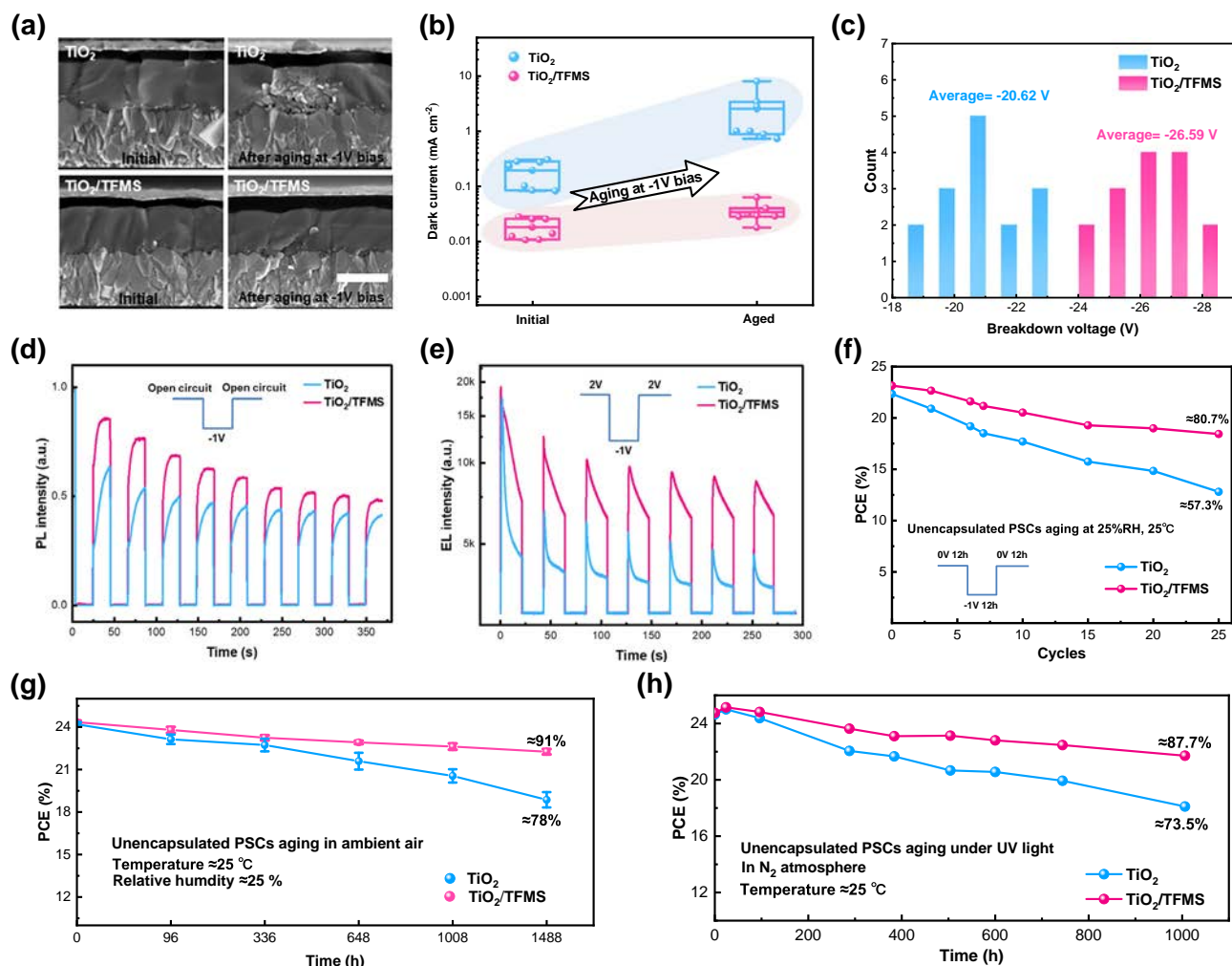
Fig. 3 | Interfacial electrostatic repulsion inhibits ion cross-layer migration. **a**, **b** Depth-profiling XPS spectra of I *3d* of without TFMS and with TFMS-based samples after −1 V bias aging 2 h. **c** ToF-SIMS depth profiles of PSCs after −1 V bias aging 2 h. **d** The interaction between TFMS and perovskite. **e** The migration path of Iˉ away from the surface of perovskite with TFMS and without TFMS. **f** The migration energy barrier of Iˉ away from the surface of perovskite with TFMS and without TFMS.

induced decomposition of perovskite. Notably, the ability to withstand reverse bias breakdown represents a critical parameter for PSCs in practical implementation[30,47–49]. Once initiated, the breakdown phenomenon induces a substantial current flow through the PSCs, generating localized high temperatures that lead to complete material decomposition and immediate device failure. The breakdown voltage of PSCs can be characterized through dark-state *J-V* measurements. Statistical analysis of breakdown voltages was performed on 15 devices. The results demonstrate that TiO₂/TFMS-based PSCs exhibit an average breakdown voltage of -26.59 V, representing a significant enhancement of ~6 V compared to conventional TiO₂-based PSCs (-20.62 V) (Fig. 4c). Notable, the TiO₂/TFMS-based PSCs achieved a maximum breakdown voltage of -28.11 V, which is higher than the reported values for single-junction PSCs (Supplementary Fig. 29 and 30, Table S5). This obtained high breakdown voltage should stand on the structural advantage of n-i-p PSCs and the efficacy of TFMS on enhancing the reverse-bias stability (Supplementary Fig. 31, Note S1). In addition, during the experiment process, we reveal that the breakdown voltage is also related to the scan speed, which emphasizes that the detailed test information is necessary to assist the analysis of breakdown voltage (Supplementary Fig. 32, Note S2).

We further studied the effect of a periodic reverse bias on the photoelectric performance of PSCs, including photoluminescence, electroluminescence, and efficiency evolution. In the open-circuit case, PSCs show a high PL intensity. Once the -1 V bias is added, the PL intensity will rapidly decay due to the carrier separation under the electric field (Fig. 4d). When the -1 V bias is withdrawn after 20 s, the PL intensity can be found to show an obvious recovery process. In the first cycle, TiO₂-based PSC can only immediately recover to ~39% of the initial PL intensity, and then slowly recover to 69% of the initial PL intensity. In contrast, TiO₂/TFMS-based PSC can immediately recover to ~70% of the initial PL intensity and rapidly stabilize at ~89% of the initial PL intensity. After 9 cycles of open circuit/-1 V/open circuit cycle,

the TiO₂/TFMS-based PSC can still maintain significantly higher PL intensity than that of the TiO₂-based PSC. When +2 V bias is applied, both types of PSCs show strong EL intensity immediately, but the TiO₂-based PSC shows more rapid attenuation over a period of 20 s of continuous pressure (Fig. 4e). When the -1 V bias is applied in the first cycle, the EL intensity of PSCs will completely disappear, and once the +2 V bias is added again, the EL strength will immediately increase again. But at this time, the TiO₂-based PSC can only recover to 38% of the initial strength, which is far lower than the 65% of the TiO₂/TFMS-based PSC. After 6 cycles of the +2 V/-1 V/ + 2 V cycle, the EL intensity that the TiO₂/TFMS-based PSC can recover is much higher than that of the TiO₂-based PSC. Both PL and EL results of TiO₂/TFMS-based PSCs show better recoverability, which is probably due to the introduction of an electrostatic repulsion layer that inhibits the Iˉ cross-layer migration. It also showed a similar improvement effect when applied to the SnO₂ ETL (Supplementary Figs. 33 and 34). We also tracked the PCE evolution of PSCs under the continuous reverse bias of -1 V and -2 V, respectively. The PCE was obtained through interrupting the applied reverse voltage and performing the *J-V* curves immediately. As shown in Supplementary Fig. 35, the PCE of the TiO₂-based PSCs decreased significantly after the first continuous reverse bias and this PCE shows no significant change after following multiple cycles of reverse bias. As a comparison, the PCE of TiO₂/TFMS-based PSCs also shows an obvious decay; however, this decay shows slight recovery after the following treatment of reverse bias. This PCE recovery may be related to the reverse migration of iodide back to perovskite. After 10 cycles of testing, both devices were restored for 6 h in the dark condition. The TiO₂-based PSCs recovered to 89.8% of their initial PCE, which was also lower than 98.5% of the TiO₂/TFMS-based PSCs. We further increased the reverse bias from -1 V to -2 V, and the results shows that the PCE of device shows an intensified decay and the PCE evolution tendency is similar with that under bias of -1 V (Supplementary Fig. 36). The results show that TFMS exerts its effect through electrostatic repulsion in a

Fig. 4 | Interface electrostatic repulsion improves PSCs' reverse bias stability. **a** The cross-section SEM of PSCs before and after −1 V bias aging for 100 h. **b** The dark current of PSCs before and after −1 V bias aging for 100 h. **c** Distribution histograms of the breakdown voltage of PSCs, 15 in each group. **d** The PL evolution of PSCs under open circuit/−1 V/open circuit cycle. **e** The EL evolution of PSCs under the +2 V/−1 V/ + 2 V cycle. **f** Bias-stability of unencapsulated PSCs under 0 V/ −1 V/0 V cyclic bias in the dark stored under ambient conditions. **g** Long-term stability of unencapsulated PSCs stored under ambient conditions. **h** UV stability of unencapsulated PSCs stored under N_2 atmosphere.

non-bonding and releasable manner, which helps to inhibit the migration of iodide ions to the ETL, promotes the reverse migration of iodide ions to the perovskite. In addition, the TFMS also possesses the ability to block holes, which can also contribute to the enhanced reverse stability of PSCs (Supplementary Figs. 36, 37 and Note S3).

We further studied the reverse bias stability of unencapsulated PSCs under 0 V/-1 V/0 V cyclic bias (each stage lasts for 12 h) in dark. As shown in Fig. 4f, after 25 cycles, the efficiency of the TiO_2-based PSC has dropped to less than 60% of the initial efficiency, while the TiO_2/ TFMS-based PSC still maintains more than 80% of the initial efficiency, demonstrating the enhanced reverse stability after constructing the interfacial electrostatic repulsion. Further, at a 0 V/-2 V/0 V bias cycle, we compared the reverse bias stability between the PSCs with/without TFMS. As shown in Supplementary Fig. 38, after 14 bias cycles, the PCE of the TiO_2-based PSCs dropped below 50% of the initial PCE, while the TiO_2/TFMS-based PSCs still maintained 72.1% of the initial PCE. The results validate the efficacy of TFMS on enhancing the device reverse-bias stability.

We also examined the PCE evolution of unencapsulated PSCs under different conditions. Firstly, as shown in Fig. 4g, after storage for 1400 h at ambient air (25 °C, 25% relative humidity), the average efficiency of TiO_2-based PSCs (5 samples in each group) decreased to 78%

of the initial average efficiency, while the TiO_2/TFMS-based PSCs could maintain 91% of the initial average efficiency. Considering the TiO_2 as the ETL, the UV stability also needs to be considered due to its photocatalytic property. After introducing TFMS on the surface of TiO_2, the device shows enhanced UV stability by maintaining 87.7% of the initial efficiency after aging for 1000 h under UV light, higher than that (73.5%) of TiO_2-based device. This enhanced UV stability may mainly result from the passivated interfacial defects[16,50].

Discussion

In summary, we have developed a strategy based on interfacial electrostatic repulsion to suppress the I⁻ cross-layer migration under reverse bias in a nonbonding manner, effectively improving the anti-reverse bias characteristics of PSCs while maintaining its high efficiency. Based on this strategy, we obtained highly efficient PSCs based on a TiO_2 ETL of 25.80% and achieved a certified PCE of 26.09% when extending applications in SnO_2 ETL. More importantly, this strategy effectively improves the reverse bias stability of the PSCs, which can maintain more than 80% of initial efficiency after 25 bias aging cycles (0 V/-1 V/0 V). In addition, the breakdown voltage of the PSCs has also been increased to a maximum of -28.11 V, which can help prevent complete failure caused by reverse breakdown in practical

applications. This work sheds light on utilizing the interfacial electrostatic repulsion to enhance the PSCs' reverse-bias stability, which is expected to accelerate the practical deployment of PSCs.

Methods

Materials

The patterned F-doped tin oxide glass (FTO, $7\,\Omega\,sq^{-1}$) was purchased from Shangyang Solar Energy Technology CO., Ltd. (Suzhou, China). Titanium tetrachloride ($TiCl_4$, 99.99%) precursor was purchased from Aladdin (Shanghai, China). Lead iodide (PbI_2, 99.999%) was purchased from Tokyo Chemical Industry (TCI). 4,4',4",4"'-methanetetrayltetrabenzenesulfonic acid (TFMS), Rubidium chloride (RbCl) was purchased from Sigma Aldrich. Polyhexamethyleneguanidine hydrochloride (PHMG, 99%) was purchased from Macklin. Tin (II) chloride dihydrate ($SnCl_2 \cdot 2H_2O$, >99.995%), urea (>99.5%), N, N- dimethylformamide (DMF), dimethyl sulfoxide (DMSO), acetonitrile (ACN), chlorobenzene (CB), guanabenz acetate salt (GBA), thioglycolic acid (TGA, 98%), and isopropanol (IPA) were purchased from Sigma-Aldrich. Formamidinium iodide (FAI), methylammonium chloride (MACl), CsI, 2,2',7,7'-tetrakis (N, N-di-pmethoxyphenylamine)-9,9'spirobifluorene (Spiro-OMeTAD), tert-butylpyridine (tBP), 2-Fluorophenylethylammonium Iodide (o-F-PEAI), 4-methoxyphenylethylamine hydroiodide (Meo-PEAI, 99.8%), Li-bis(trifluoromethanesulfonyl)imid (Li-TFSI), and Iodobenzene diacetate (ID, 99.99%) were purchased from Xi'an Yuri Solar CO., Ltd.

Device fabrication

The FTO substrates were ultrasonically cleaned in the sequence of detergent solution, deionized water, ethanol, and deionized water for 15 min, respectively.

For TiO_2 ETL: A mixture of $TiCl_4$ (4 ml) and deionized water (200 ml) was stirred to obtain a TiO_2 precursor. The FTO substrate was then immersed in the precursor and placed in a water bath at 70 °C for 40 min to form a compact TiO_2 ETL. After the preparation is complete, the compact TiO_2 ETL is removed from the chemical bath precursor, and the surface is washed with deionized water, ethanol, and deionized water successively to remove impurities and then dried with N_2 for use.

For $FTO/TiO_2/TFMS$ substrate: the TFMS precursor (0.3 mg/ml in deionized water) were spin-coated on FTO/TiO_2 substrate at 4000 rpm for 30 s, and followed by the annealing at 100 °C for 10 min.

Preparation of perovskite by one-step method: The 1.54 M $FA_{0.85}MA_{0.1}Cs_{0.05}PbI_3$ (DMF: DMSO, 4:1 volume/volume) precursor containing 0.06 mg/ml rubidium chloride and 1.2 mg/ml PHMG additives were spin-coated on FTO/TiO_2 or $FTO/TiO_2/TFMS$ substrate at 4000 rpm for 18 s, 800 µl diethyl ether as anti-solvent was dripped at 12 s before the end of spin-coating. Then, the film was transferred to air (25 °C & 35% RH) for annealing at 110 °C for 10 min. The Meo-PEAI solution was prepared by mixing 4.5 mg Meo-PEAI in 1 ml CB: IPA mixed solvent (4:1 volume/volume). The Meo-PEAI layer was spin-coated at 4000 rpm for 30 s above the perovskite. The Spiro-OMeTAD solution was prepared by mixing 72.3 mg Spiro-OMeTAD in 1 ml chlorobenzene with 26.6 µl tBP, 18 µl Li-TFSI salt (520 mg ml^{-1} in ACN), and 1 mg ID. The Spiro-OMeTAD solution was spin-coated at 4000 rpm for 30 s above the perovskite layer. At last, Au electrode (60 nm) was deposited by thermal evaporation.

Preparation of the SnO_2 ETL: 1.1 g $SnCl_2 \cdot 2H_2O$ (~12 mM) and 5 g urea were dissolved in 400 mL deionized water, and then 5 mL HCl (37 wt%) and 100 µL TGA were added into the solution. The as-cleaned FTO was placed vertically into the SnO_2 CBD solution and heated in a drying oven at 90 °C for 4 h. Then, sequentially ultrasonicated with deionized water and isopropanol for five min, dried by gas gun blowing, and followed by annealing at 150 °C for 1 h.

For $FTO/SnO_2/TFMS$ substrate: the TFMS precursor (0.1 mg/ml in deionized water) was spin-coated on FTO/SnO_2 substrate at 4000 rpm for 30 s, and followed by annealing at 100 °C for 10 min.

Preparation of perovskite via the two-step method in ambient air: a 1.5 M PbI_2 (DMF: DMSO, 9:1 volume/volume) precursor with guanabenz acetate (the molar ratio of GBA/PbI_2 was 3%) was spin coated on the FTO/SnO_2 or $FTO/SnO_2/TFMS$ substrate at 1500 rpm for 30 s and then annealed at 70 °C for 60 s. After the PbI_2 film cooled to room temperature, ammonium salt solution was spin-coated on the PbI_2 film at 2000 rpm. for 30 s and then annealed at 150 °C for 15 min. Then, o-F-PEAI solution was spin-coated on the FTO/SnO_2/perovskite surface at 4000 rpm for 30 s without further annealing. The Spiro-OMeTAD solution was prepared by mixing 72.3 mg Spiro-OMeTAD in 1 ml chlorobenzene with 26.6 µl tBP, 18 µl Li-TFSI salt (520 mg ml^{-1} in ACN), and 1 mg ID. The Spiro-OMeTAD solution was spin-coated at 4000 rpm for 30 s above the perovskite layer. At last, Au electrode (60 nm) was deposited by thermal evaporation.

Characterization

The surface and cross morphologies of perovskite films were measured using cold field-emission scanning electron microscopy (SEM, HITACHI Regulus 8100). The X-ray diffractometer (XRD, D8 Advance, Bruker) obtained crystalline perovskite films. Steady-state PL and time-resolved PL were performed by a FLS980 spectrometer (Edinburgh Instrument). The excitation wavelength is 470 nm. The J-V test was measured using a Keithley 2400 source meter under simulated AM 1.5 G illumination (100 mW cm^{-2}) provided by a 150 W Class AAA solar simulator (XES-40S1, SAN-EI). The scanning range of the J-V test was -0.1 to 1.2 V, the scanning speed was 0.06 V s^{-1}, and the number of scanning points was 100, with a step size is 0.013 V. When conducting the reverse bias scans to determine the breakdown voltage, the scanned voltage was from +1.2 V to -30 V at a scanning speed of -4 V/s. The external quantum efficiency and integrating current of perovskite solar cells were measured by QE-R systems (Enli Tech). The unpackaged devices were stored in ambient air at room temperature (25 °C, 25% RH) to measure the long-term aging stability. Bias-stability of unencapsulated PSCs under 0 V/-1 V/0 V cyclic bias in the dark, stored under ambient air (25 °C, 25% RH). The UV stability of unencapsulated PSCs was tested under 25 °C in an N_2 glovebox. The electrochemical impedance spectroscopy (EIS) data were obtained by an electrochemical workstation (Zahner Zennium). Impedance spectra were measured using HIOKI impedance analyzer (IM 3570). Time-of-flight secondary ion mass spectrometry (TOF-SIMS 5-100, IONTOF GmbH) was performed to characterize the ionic migration. Transient ion-migration current was obtained by electrochemical workstation (CHI660E). X-ray photoelectron spectroscopy (XPS) and Ultraviolet photoelectron spectroscopy (UPS) were performed using an ESCALAB 250Xi system to analyze the surface composition and electronic structure of the samples. Atomic force microscopy (AFM) using an FMNanoview 1000 instrument was used to characterize the surface morphology of the samples. Kelvin probe force microscopy (KPFM) was utilized to measure the surface potential and contact current of the films. The Zeta potential on the surface of films were measured using SurPASS2. In-situ PL and EL tests were performed by a dynamic spectrometers come from Shaanxi Puguangweishi Technology Co.,Ltd.

The static diffusion experiment of polyiodide ions

The static diffusion experiment of polyiodide ions was designed by referring to the relevant literature on zinc-iodine batteries[39,51]. The static diffusion experiment of polyiodides ions was conducted using the H-type electrolytic cells, in which equal amounts of polyiodides solution and deionized water are added to the left and right chambers, and the two chambers are separated by Glass fiber (GF) diaphragm without TFMS and GF diaphragm with TFMS, respectively. The polyiodides solution was prepared by dissolving 5 mM I_2 into 0.2 M KI aqueous solutions. GF diaphragm was purchased from Beijing Shenheweiye Technology Co., Ltd. For the GF diaphragm with TFMS, the TFMS

powder was first dissolved in acetonitrile solvent with a concentration of 20 mg mL^{-1}, and then the GF diaphragm was immersed into the TFMS-acetonitrile solution for 10 min. After that, the obtained GF diaphragm with TFMS was dried under 50 °C for 12 h. For the GF diaphragm without TFMS, the glass fiber diaphragm was immersed into the pure acetonitrile solution for 10 min. After that, the obtained GF diaphragm without TFMS was dried under 50 °C for 12 h. The processed and dried GF diaphragms were used in the aforementioned static diffusion test of polyiodides.

DFT Calculations
We used the DFT as implemented in the Vienna Ab initio simulation package (VASP) in all calculations. The exchange-correlation potential is described by using the generalized gradient approximation of Perdew-Burke-Ernzerhof (GGA-PBE). The projector augmented-wave (PAW) method is employed to treat interactions between ion cores and valence electrons. The plane-wave cutoff energy was fixed to 450 eV. Given structural models were relaxed until the Hellmann–Feynman forces smaller than -0.02 eV/Å and the change in energy smaller than 10^{-5} eV was attained. Grimme's DFT-D3 methodology was used to describe the dispersion interactions among all the atoms in adsorption models. The Gamma-centered k-points samplings were set with a density of 0.04. The Climbing Image Nudged Elastic Band (CI-NEB) method was employed to compute the corresponding barrier heights of Li diffusion in the electrolyte. Gauss computation part: all calculations were performed using the Gaussian 16 program package. The M06-2X hybrid Functional combine with Def2-SVP was used to optimize the structures and M06-2X combined with Def2-TZVP was used for single-point calculations. All post-calculation analysis was carried out using the Multiwfn 3.8.4 Dev software package and the results were visualized using visual molecular dynamics (VMD) 1.8. 4.

Reporting summary
Further information on research design is available in the Nature Portfolio Reporting Summary linked to this article.

Data availability
All data generated in this study are provided in the article and Supplementary Information and the raw data supporting this study are available from the Source Data file. Source data are provided with this paper.

References
1. Best research-cell efficiency chart: https://www.nrel.gov/pv/cell-efficiency. (2025).
2. Green, M. A. et al. Solar cell efficiency tables (Version 65). *Prog. Photovoltaics: Res. Appl.* **33**, 3–15 (2025).
3. Li, S. et al. High-efficiency and thermally stable FACsPbI$_3$ perovskite photovoltaics. *Nature* **635**, 82–88 (2024).
4. Liu, Z. et al. All-perovskite tandem solar cells achieving >29% efficiency with improved (100) orientation in wide-bandgap perovskites. *Nat. Mater.* **24**, 252–259 (2025).
5. Zhuang, J. et al. Review on chemical stability of lead halide perovskite solar cells. *Nano-Micro Lett.* **15**, 84 (2023).
6. Khenkin, M. V. et al. Consensus statement for stability assessment and reporting for perovskite photovoltaics based on ISOS procedures. *Nat. Energy* **5**, 35–49 (2020).
7. Liu, X. et al. Stabilization of photoactive phases for perovskite photovoltaics. *Nat. Rev. Chem.* **7**, 462–479 (2023).
8. Fei, C. et al. Strong-bonding hole-transport layers reduce ultraviolet degradation of perovskite solar cells. *Science* **384**, 1126–1134 (2024).
9. Wang, C. et al. Perovskite solar cells in the shadow: Understanding the mechanism of reverse-bias behavior toward suppressed reverse-bias breakdown and reverse-bias induced degradation. *Adv. Energy Mater.* **13**, 2203596 (2023).
10. Baumann, S. et al. Stability and reliability of perovskite containing solar cells and modules: degradation mechanisms and mitigation strategies. *Energy Environ. Sci.* **17**, 7566–7599 (2024).
11. Yan, L. et al. Fabrication of perovskite solar cells in ambient air by blocking perovskite hydration with guanabenz acetate salt. *Nat. Energy* **8**, 1158–1167 (2023).
12. Ma, Y. et al. Suppressing ion migration across perovskite grain boundaries by polymer additives. *Adv. Funct. Mater.* **31**, 2006802 (2021).
13. Azam, M. et al. Tailoring pyridine bridged chalcogen-concave molecules for defects passivation enables efficient and stable perovskite solar cells. *Nat. Commun.* **16**, 602 (2025).
14. Mariani, P. et al. Low-temperature strain-free encapsulation for perovskite solar cells and modules passing multifaceted accelerated ageing tests. *Nat. Commun.* **15**, 4552 (2024).
15. Qu, S. et al. Revealing and inhibiting the facet-related ion migration for efficient and stable perovskite solar cells. *Angew. Chem. Int. Ed.* **64**, e202415949 (2025).
16. Huang, H. et al. 24.8%-efficient planar perovskite solar cells via ligand-engineered TiO$_2$ deposition. *Joule* **6**, 2186–2202 (2022).
17. Zhong, Y. et al. Inhibition of ion migration for highly efficient and stable perovskite solar cells. *Adv. Mater.* **35**, 2302552 (2023).
18. Thiesbrummel, J. et al. Ion-induced field screening as a dominant factor in perovskite solar cell operational stability. *Nat. Energy* **9**, 664–676 (2024).
19. Jeangros, Q. et al. In situ TEM analysis of organic–inorganic metal-halide perovskite solar cells under electrical Bias. *Nano Lett.* **16**, 7013–7018 (2016).
20. Ni, Z. et al. Evolution of defects during the degradation of metal halide perovskite solar cells under reverse bias and illumination. *Nat. Energy* **7**, 65–73 (2022).
21. Bowring, A. R. et al. Reverse bias behavior of halide perovskite solar cells. *Adv. Energy Mater.* **8**, 1702365 (2018).
22. Rizzo, A. et al. Understanding lead iodide perovskite hysteresis and degradation causes by extensive electrical characterization. *Sol. Energy Mater. Sol. Cells* **189**, 43–52 (2019).
23. Jia, S. et al. Ion-accumulation-induced charge tunneling for high gain factor in p–i–n-structured perovskite CH$_3$NH$_3$PbI$_3$ X-ray detector. *Adv. Mater. Technol.* **7**, 2100908 (2022).
24. Ren, X. et al. Mobile iodides capture for highly photolysis- and reverse-bias-stable perovskite solar cells. *Nat. Mater.* **23**, 810–817 (2024).
25. Xiong, Q. et al. Rear interface engineering to suppress migration of iodide ions for efficient perovskite solar cells with minimized hysteresis. *Adv. Funct. Mater.* **32**, 2107823 (2022).
26. Li, N. et al. Barrier reinforcement for enhanced perovskite solar cell stability under reverse bias. *Nat. Energy* **9**, 1264–1274 (2024).
27. Lanzetta, L. et al. Tin–lead perovskite solar cells with enhanced reverse bias stability. *ACS Energy Lett.* **10**, 2093–2095 (2025).
28. Yang, Q. et al. Mobile oxygen capture enhances photothermal stability of perovskite solar cells under ISOS protocols. *Adv. Mater.* **37**, 2500268 (2025).
29. Zhao, T. et al. Cesium lead chloride nanocrystals interface blocking layer enables stable and efficient perovskite solar cells. *Adv. Funct. Mater.* **n/a**, 2421104 (2025).
30. Bogachuk, D. et al. Perovskite Photovoltaic Devices with Carbon-Based Electrodes Withstanding Reverse-Bias Voltages up to –9 V and Surpassing IEC 61215:2016 International Standard. *Sol. RRL* **6**, 2100527 (2022).
31. Fan, W. et al. Grain boundary perfection enabled by pyridinic nitrogen doped graphdiyne in hybrid perovskite. *Adv. Funct. Mater.* **31**, 2104633 (2021).
32. Zhang, Y. et al. Improved fatigue behaviour of perovskite solar cells with an interfacial starch–polyiodide buffer layer. *Nat. Photonics* **17**, 1066–1073 (2023).

33. Liu, N. et al. Columnar macrocyclic molecule tailored grain cage to stabilize inorganic perovskite solar cells with suppressed halide segregation. *Adv. Energy Mater.* **14**, 2402443 (2024).

34. Jiang, C. et al. Double layer composite electrode strategy for efficient perovskite solar cells with excellent reverse-bias stability. *Nano-Micro Lett.* **15**, 12 (2022).

35. Wan, Z. et al. Suppressing ion migration through dual interface engineering toward efficient and stable perovskite solar modules. *ACS Energy Lett.* **10**, 1585–1595 (2025).

36. Xiao, M. et al. Engineering amorphous–crystallized interface of ZrN barriers for stable inverted perovskite solar cells. *Adv. Mater.* **35**, 2301684 (2023).

37. Gao, D. et al. Long-term stability in perovskite solar cells through atomic layer deposition of tin oxide. *Science* **386**, 187–192 (2024).

38. Chen, Z.-F. et al. A functionalized membrane for lithium–oxygen batteries to suppress the shuttle effect of redox mediators. *J. Mater. Chem. A* **7**, 14260–14270 (2019).

39. Lin, P. et al. Simultaneous inhibition of Zn dendrites and polyiodide ions shuttle effect by an anion concentrated electrolyte membrane for long lifespan aqueous zinc–iodine batteries. *ACS Nano* **17**, 15492–15503 (2023).

40. Zhang, L. et al. Tuning ion transport at the anode-electrolyte interface via a sulfonate-rich ion-exchange layer for durable zinc-iodine batteries. *Adv. Energy Mater.* **13**, 2203790 (2023).

41. Qi, J. et al. Modulating dual functionalities of hydrazide derivatives for iodide oxidation suppression and defect passivation in printable mesoscopic perovskite solar cells. *Adv. Energy Mater.* **14**, 2402344 (2024).

42. Hu, Z. et al. Crowding effect-induced zinc-enriched/water-lean polymer interfacial layer toward practical Zn-Iodine batteries. *ACS Nano* **17**, 23207–23219 (2023).

43. Krogmeier, B. et al. Quantitative analysis of the transient photoluminescence of $CH_3NH_3PbI_3$/PC61BM heterojunctions by numerical simulations. *Sustain. Energy Fuels* **2**, 1027–1034 (2018).

44. Al-Ashouri, A. et al. Monolithic perovskite/silicon tandem solar cell with >29% efficiency by enhanced hole extraction. *Science* **370**, 1300–1309 (2020).

45. Lu, T. & Chen, Q. Independent gradient model based on Hirshfeld partition: a new method for visual study of interactions in chemical systems. *J. Comput. Chem.* **43**, 539–555 (2022).

46. Liu, F. et al. Functional design and understanding of effective additives for achieving high-quality perovskite films and passivating surface defects. *J. Energy Chem.* **102**, 597–608 (2025).

47. Najafi, L. et al. Reverse-bias and temperature behaviors of perovskite solar cells at extended voltage range. *ACS Appl. Energy Mater.* **5**, 1378–1384 (2022).

48. Wang, C. et al. Abnormal dynamic reverse bias behavior and variable reverse breakdown voltage of ETL-free perovskite solar cells. *Sol. RRL* **7**, 2300456 (2023).

49. Jiang, F. et al. Improved reverse bias stability in p–i–n perovskite solar cells with optimized hole transport materials and less reactive electrodes. *Nat. Energy* **9**, 1275–1284 (2024).

50. Ji, J. et al. Two-stage ultraviolet degradation of perovskite solar cells induced by the oxygen vacancy-Ti^{4+} states. *iScience* **23**, 101013 (2020).

51. Yuan, W. et al. Polycationic polymer functionalized separator to stabilize aqueous zinc-iodine batteries. *Energy Storage Mater.* **76**, 104130 (2025).

Acknowledgements

Author contributions

M.L., Z.L., and H.H. conceived the idea. M.L., H.H., and P.C. guided the work as supervisors. Z.L. and Y.Y. did experimental designs, device fabrication, and data analysis. S.D. participated in the device fabrication and some characterizations. Q.Z. and Z.W. assisted with some characterization tests. T.J., C.S., and L.L. contributed to the ion migration characterization. Z.L. S.Q., and H.H. wrote the first draft of the manuscript. L.Y. and Y.Y. assisted in revision and polishing the manuscript language. All authors discussed the results and contributed to the revisions of the manuscript.

Competing interests

The authors declare no competing interests.

Additional information

Supplementary information The online version contains supplementary material available at https://doi.org/10.1038/s41467-025-66224-7.

Correspondence and requests for materials should be addressed to Hao Huang or Meicheng Li.

Peer review information *Nature Communications* thanks Yongbo Yuan, and the other, anonymous, reviewer(s) for their contribution to the peer review of this work. A peer review file is available.

Reprints and permissions information is available at http://www.nature.com/reprints

Publisher's note Springer Nature remains neutral with regard to jurisdictional claims in published maps and institutional affiliations.